

High-throughput, subpixel precision analysis of bacterial morphogenesis and intracellular spatio-temporal dynamics

Oleksii Sliusarenko,^{1,3} Jennifer Heinritz,³
Thierry Emonet^{1,2*} and Christine Jacobs-Wagner^{1,3,4*}

Departments of ¹Molecular, Cellular and Developmental Biology and ²Physics, Yale University, New Haven, CT 06520, USA.

³Howard Hughes Medical Institute, Yale University, New Haven, CT 06520, USA.

⁴Section of Microbial Pathogenesis, Yale School of Medicine, New Haven, CT 06510, USA.

Summary

Bacteria display various shapes and rely on complex spatial organization of their intracellular components for many cellular processes. This organization changes in response to internal and external cues. Quantitative, unbiased study of these spatio-temporal dynamics requires automated image analysis of large microscopy datasets. We have therefore developed MicrobeTracker, a versatile and high-throughput image analysis program that outlines and segments cells with subpixel precision, even in crowded images and mini-colonies, enabling cell lineage tracking. MicrobeTracker comes with an integrated accessory tool, SpotFinder, which precisely tracks foci of fluorescently labelled molecules inside cells. Using MicrobeTracker, we discover that the dynamics of the extensively studied *Escherichia coli* Min oscillator depends on Min protein concentration, unveiling critical limitations in robustness within the oscillator. We also find that the fraction of MinD proteins oscillating increases with cell length, indicating that the oscillator has evolved to be most effective when cells attain an appropriate length. MicrobeTracker was also used to uncover novel aspects of morphogenesis and cell cycle regulation in *Caulobacter crescentus*. By tracking filamentous cells, we show that the chromosomal origin at the old-pole is responsible for most replication/separation events while the others remain largely silent despite contiguous cytoplasm. This surprising position-dependent silencing is regulated by division.

Accepted 1 February, 2011. *For correspondence. E-mail thierry.emonet@yale.edu or christine.jacobs-wagner@yale.edu; Tel. (+1) 203 432 5170; Fax (+1) 203 432 6161.

Introduction

Contrary to earlier belief, bacteria possess various cytoskeletal elements, exhibit polarity, localize proteins at specific cellular locations, organize lipids in spatial domains and position their chromosome and transcripts in a defined and predictable fashion (Shapiro and Losick, 2010). This surprisingly sophisticated cellular organization, which can change in response to cell cycle progression, growth conditions, chemical perturbations, cellular age or mutations, impacts most aspects of bacterial physiology and behaviour. As a consequence, the importance of imaging in bacterial research has drastically increased over the last two decades (Shapiro and Losick, 2010). This enterprise has been fuelled by the development of new microscopy techniques and new fluorescent probes, both chemical and genetically encoded, targeting various cellular components and sub-cellular structures. Modern automated microscopes have the capability of obtaining large amounts of data by screening multiple markers in large cell populations. This, in turn, has resulted in a need for quantitative automated analysis methods that can process large datasets and generate statistically meaningful measurements in a precise and unbiased manner. The need for such methods dramatically increases with the use of time-lapse imaging, in which the same cells are imaged over time. An increase of cell density and clustering in experimental samples (for the sake of obtaining more data and/or as a result of cell division and mini-colony formation on the slide) makes automated cell identification particularly challenging.

There are currently multiple image analysis programs capable of cell detection, although most of them work best with eukaryotic cells. Bacterial cells are comparatively small in size, often close to the resolution of optical microscopy, making it challenging to use standard pixel-based techniques to separate clusters of cells and to obtain the required subpixel precision. A few image analysis tools have been used for bacterial cells, which typically start with image thresholding in order to outline bright or dim cells against a uniform background, produced using either phase contrast microscopy or fluorescence microscopy of uniformly labelled cells (Guberman *et al.*, 2008; Locke and Elowitz, 2009; Christen *et al.*, 2010a). These programs can be categorized into two groups based on

their approaches. One focuses on maximizing resolution of cell outlines by utilizing interpolation between pixel values (Guberman *et al.*, 2008). This method produces high precision cell contours in well-separated cells but fails to identify touching or hard-to-resolve cells, preventing analysis of densely packed cells in still images as well as progeny in time-lapse images of dividing cells. The other group of methods used for bacterial cells focuses on segmenting the image to separate densely packed cells at the expense of precision by using pixel-based operations, such as edge detection, watershed, and morphological erosion and dilation (Locke and Elowitz, 2009; Christen *et al.*, 2010a; Wang *et al.*, 2010b). However, there is a strong demand for the capability of obtaining subpixel precision outlines of touching cells in noisy images while increasing automation of the process.

These tasks can, in principle, be achieved by implementing some of the concepts and algorithms developed for medical image segmentation and computer vision, which include clustering, template-matching, active contours, region growing and level set methods (Pham *et al.*, 2000). In this work, we describe a new cell detection program, named MicrobeTracker, which combines several of these methods and utilizes cell shape and time-lapse information when available to achieve high precision cell outlining even in densely packed and noisy images, allowing for automated outlining and subsequent analysis of cells in both still images and time-lapse sequences. We also present an accessory tool, called SpotFinder, which detects small round spots, generating precise cell coordinates of fluorescently labelled foci inside cells.

We use various examples to demonstrate the performance and versatility of MicrobeTracker and to illustrate how different features of the program can be used to acquire new biological information. For instance, we show how the high precision and automation of our method can detect small, but statistically significant, asymmetries in bacterial cell shapes, revealing unsuspected cell morphogenetic properties. MicrobeTracker can also track fluorescently labelled molecules in cell lineages over several generations or in difficult-to-resolve samples, such as densely packed or filamentous cells, from time-lapse sequences. This property was exploited to gain quantitative insight into novel aspects of cell cycle regulation in *Caulobacter crescentus* and to uncover previously unknown properties and dependencies for the well-studied Min oscillator in *Escherichia coli*.

Results and discussion

MicrobeTracker and SpotFinder programs

A detailed user-oriented description of the programs as well as explanations for the choice of the major algorithms

is available in the *Experimental procedures* section. A technical description of all used algorithms is provided in the *Supporting information*.

MicrobeTracker can detect cells in phase contrast images, images of diffuse fluorescent dyes inside cells, and differential interference contrast images (the latter after pre-processing and with limitations; see *Supporting information*). The program applies a two-stage approach for cell detection. The first stage consists of pixel-based operations. At this stage, the program separates cells (or cell clusters) from the background, after which it further segments cell clusters by applying algorithms based on edge-detection and watershed transform (Figs 1A and S1). These methods efficiently separate individual cells, even within mini-colonies, producing initial guesses for their shapes, although they still lack subpixel precision or an ability of using cell history to aid detection.

The crude cell outlines produced after the first stage are refined during the second stage using a variant of active contour models (Kass *et al.*, 1988). These methods describe the shape of an individual cell with a contour, which is adjusted smoothly under the action of so-called image forces until it converges to the shape of the actual cell in the image (Fig. 1B). The contour must also obey internal constraints to ensure that the detected objects correspond to cells and that the shape of the objects is within the range of realistic cell shapes. For example, one of such constraints may be contour smoothness. We developed two different algorithms that implement active contour models, the advantages and limitations of which are described in the *Experimental procedures*.

MicrobeTracker is even more powerful when used to analyse time-lapse sequences of growing cells. It takes advantage of the additional time-dependent information to resolve complicated images, which becomes important as cell clustering increases with repeated divisions. In this case, for each time frame, the original guess of the shape is taken from the previous frame (Fig. 1C; see *Supporting information*). This approach ensures the identity of each cell over time, allowing the program to trace the history and genealogy of the cells. The program also keeps track of the identity of each cell pole (i.e. the 'new' pole created by the last division versus the 'old' pole generated by an earlier division event; see below for examples).

Once the cells have been outlined in still or time-lapse images, the program creates a mesh in each cell, which consists of a centreline and a series of 'ribs' equidistantly spaced at predefined intervals (usually 1 pixel), such that the centreline crosses each rib at a right angle (Fig. 1B). The mesh effectively creates a co-ordinate system, in which each point is described by two coordinates: its distance from the cell pole and its signed distance from the centreline. The mesh (Fig. 1B) enables quantification of individual cell shape parameters (e.g. cell width, length

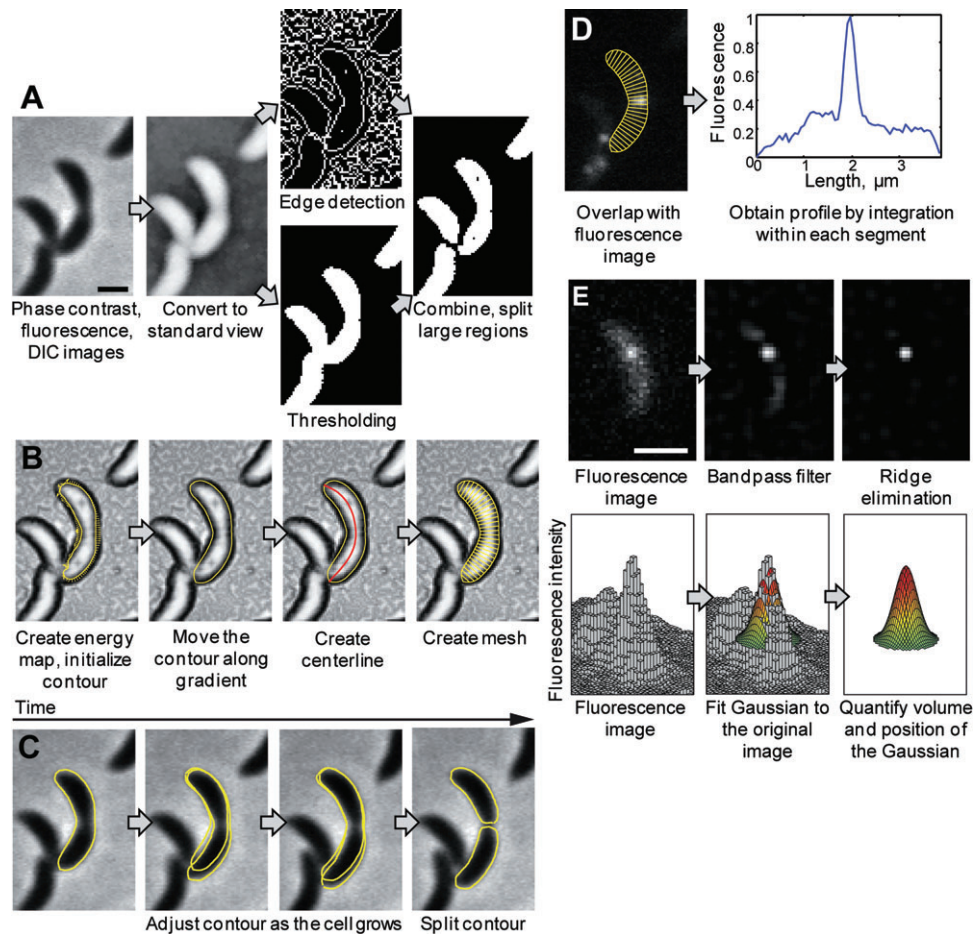


Fig. 1. Principles of MicrobeTracker operation.

A. Image preparation and the sequence of morphological operations with inversion, thresholding, edge and detection algorithms are shown. A phase contrast image of *C. crescentus* cells (MT196) expressing *ftsZ-yfp* is shown as an example. Bar: 1 μm .

B. Active contour model and cell mesh generation. First, the energy map is generated (shown as the background), which is converted to forces (shown as arrows) and used to move a constraint active contour. The fit is considered converged when the forces drop below a certain magnitude or after a fixed number of steps. The mesh generation starts from the centreline determination and results in a creation of a set of segments of equal length along the curved cell body.

C. Cell contour determination in time-lapse sequences. The active contour starts using its position from the previous frame and adjusts to the new position and shape of the cell. After that, the program checks whether the cell has divided and if so, splits the contour.

D. A fluorescence profile of FtsZ-YFP signal is calculated by integration of the signal in each segment, after which the intensity can be normalized by the area or volume of the segment.

E. The principles of SpotFinder operation. Top left, original fluorescence image (LacI-CFP bound to a *lacO* array at the chromosomal terminus; strain MT16). Top centre, the same image after processing with a bandpass filter. Top right, the same image after further processing with the ridge-removal routine. Bottom, this processed image is then used to obtain an initial guess of the position, width and height of the spots, and finally a 2D Gaussian is fit to the original image. Bar: 1 μm .

and curvature) as well as measurements of growth rate and cell division (e.g. timing, positioning and degree of cell constriction). Precise measurements of individual cell shapes in large image datasets can identify small but statistically significant features of cell morphogenesis, which otherwise would be buried in measurement noise. We illustrated this point by quantifying the length and width of 5200 dividing cells in an asynchronous population of *C. crescentus*, a dimorphic bacterium that divides asymmetrically to produce a flagellated 'swarmer' cell slightly shorter than its sibling, the so-called 'stalked' cell.

Using MicrobeTracker, constricting cells were automatically identified and oriented using the old-pole marker DivJ kinase fused to YFP (Fig. 2A–C). Consistent with established knowledge (Terrana and Newton, 1975; Quardokus and Brun, 2002; Schofield *et al.*, 2010), length measurements showed that the division plane was asymmetrically positioned with the ratio between the old-pole ('stalked') and new-pole ('swarmer') sides being 1.168 ± 0.005 (mean \pm SEM) (Fig. 2D). Width measurements unexpectedly revealed a significant asymmetry as well (Fig. 2E) with the ratio between the 'stalked' and

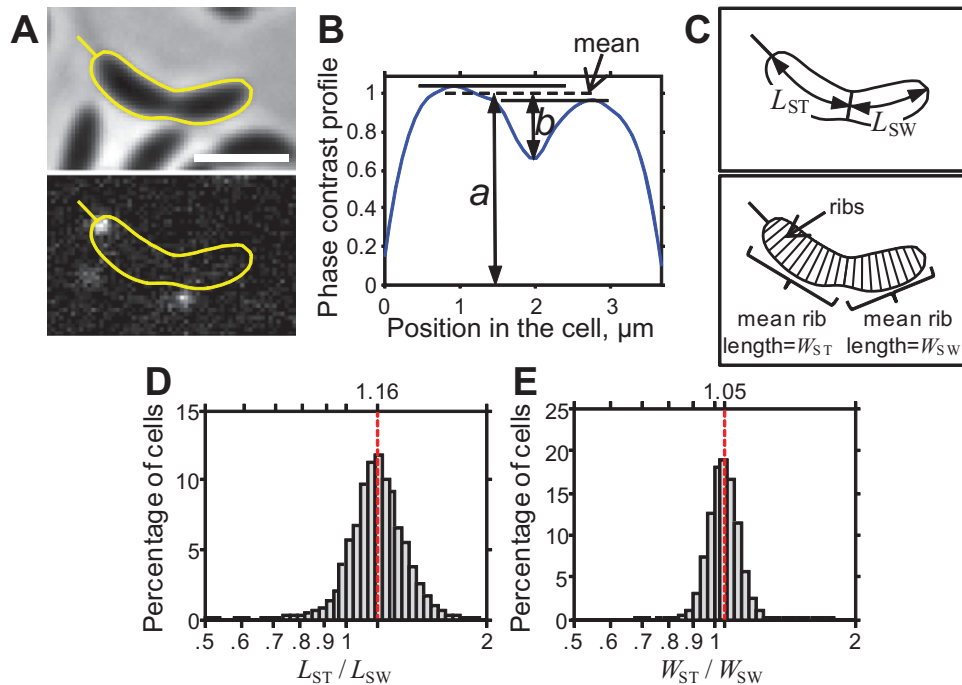


Fig. 2. Shape analysis of constricting *C. crescentus* cells. Here a *C. crescentus* strain expressing DivJ-YFP was used (strain CJW826) in order to automatically identify the old-pole of the cell where DivJ-YFP forms a tight focus. We imaged a sample of cells harvested from an exponential phase culture (14 frames, 29789 cells) and identified predivisional (constricting) cells (5200 cells). A. An example of a dividing cell outlined with MicrobeTracker. A phase contrast (top) and a CFP fluorescence (bottom) images are shown. The line extending from the pole indicates the old-pole where DivJ-CFP localizes. Bar: 2 μm . B. Phase contrast intensity profile for the cell in A. The degree of constriction is defined as b/a and had to be above 0.2 (arbitrary chosen) for the cell to be considered constricting. C. Determination of the swarmer and stalked length and width of the cell used as an example in (A). The stalked (L_{ST}) and swarmer (L_{SW}) lengths are defined as the distance along the centreline from the old- or new-pole, respectively, to the lowest point of the cell profile. The stalked (W_{ST}) and swarmer (W_{SW}) widths are defined as the mean length of the 'ribs', confined within each of the two sections of the cell. D. Histogram of the ratio between the stalked and swarmer lengths (L_{ST}/L_{SW}) with the stalked length defined as the distance between the constriction site and the old-pole while the swarmer length represents the distance between the constriction site and the new-pole (mean ratio is 1.168 ± 0.005) (mean \pm SEM). E. Histogram of the ratio between the stalked and swarmer widths, displaying a small but statistically significant asymmetry (mean ratio is 1.050 ± 0.002).

'swarmer' cell widths being 1.050 ± 0.002 . Thus, the swarmer cell side is not only $\sim 17\%$ shorter but also $\sim 5\%$ thinner than the stalked cell side, implying the existence of a cell morphogenetic program that accounts for this difference.

In addition to cell geometry, the program can extract spatial information of fluorescently labelled molecules by transferring the cell mesh from, for example, phase contrast images to corresponding fluorescence images and by integrating the fluorescence intensity in each segment created by the ribs and the cell contour. The fluorescence intensity can be plotted as a function of the position in a cell (Fig. 1D) and normalized, when needed, by the area or volume of each segment to yield the mean image brightness or mean concentration estimate in a given position within the cell (Fig. S2). This information can be used to quantify the spatial distribution of labelled molecules inside cells.

Many proteins, mRNAs, DNA regions, and other molecules appear localized in small round clusters or foci by conventional optical microscopy, making their precise localization an important task in image analysis. To achieve it, we developed an accessory program, named SpotFinder, which performs different filtering algorithms to identify round or diffraction-limited spots and to position them at subpixel resolution relative to the two-dimensional (2D) cell co-ordinate system created by MicrobeTracker (Fig. 1E; see *Experimental procedures* and *Supporting information* for a full description of the program). Examples of applications are provided below.

Tracking molecules in cell lineages: FtsZ ring dynamics in a dimorphic bacterium

Tracking the fate of specific factors in cell lineages in time-lapse experiments is highly desirable for studying

cellular aging, cell differentiation, asymmetric division and other aspects of inheritance. To illustrate the performance of MicrobeTracker with time-lapse image series across several generations, we followed the localization of the cell division protein FtsZ fused to YFP in swarmer and stalked cell lineages of *C. crescentus*. Cells were imaged every 10 min for approximately four generations (~ 8.5 h). As shown in Fig. 3A for selected time points, the program reliably outlined all the progeny (see also Movie S1). At each time point, the outline was overlapped onto the fluorescence signal from FtsZ-YFP (Fig. 3B). The program saves the numbers of each cell's 'parents' and 'progeny', and orients every cell from old-pole to new-pole following the first division (as the last division automatically identifies the new cell poles, hence circumventing the need of an old-pole or new-pole molecular marker for cell pole identification). These data were used to reconstruct the profile of the FtsZ-YFP signal for all the progeny by connecting individual cells at the poles where the division had last occurred. These profiles are shown for selected time points in Fig. 3C, and a kymographic representation of these profiles for each available time point is shown in Fig. 3D. From the analysis of 19 original cells followed for about four generations, we showed that formation of the cytokinetic FtsZ ring (determined by FtsZ-YFP localization near midcell) generally occurs sooner in stalked cells than in swarmer cells (Fig. 3E), as expected. However, we found that once the FtsZ ring is formed, the cell division program proceeds at the same pace in both cell types (Fig. 3F).

The advantages of the time-lapse tracking approach (i.e. using information from previous frames) include not only automated identification of cell type (swarmer versus stalked progeny) and cell pole (new versus old), but also increased quality and reliability of cell outlining and detection, as illustrated in Fig. 3G–K. Figure 3G shows a mini-colony formed from a single ancestor after 8.3 h of growth. *C. crescentus* cells are quite pliable and easily deformed, explaining difficulties in cell outline recognition even by eye. Nevertheless, MicrobeTracker could outline these cells when followed in a time-lapse sequence (Fig. 3H). When only thresholding was used, the cell separation was poor (Fig. 3I), which was only partially improved by edge detection (Fig. 3J). Hence, combining thresholding and edge detection without using information from the previous frames resulted in recognition of some, but not all, cells in this mini-colony (Fig. 3K).

We anticipate that time-lapse tracking experiments will become increasingly important in the bacterial cell biology field, notably because of the recent recognition that many bacterial species once thought to produce identical daughter cells in fact divide asymmetrically, yielding daughter cells with distinct cellular and behavioural characteristics (Lam *et al.*, 2003; Hallez *et al.*, 2004; Christen

et al. 2010b). Experiments of this type have already been proven useful in examining cellular senescence (Ackermann *et al.*, 2003; Stewart *et al.*, 2005; Wang *et al.*, 2010a) and in uncovering cell-to-cell fluctuations in cellular components or gene expression within clonal populations (Locke and Elowitz, 2009).

Quantifying oscillatory behaviours: MinD dynamics as a function of cell length and MinD concentration

Self-organizing systems play a vital role in driving spatio-temporal organization in both prokaryotic and eukaryotic cells. We next demonstrated the usefulness of our program on the well-studied *E. coli* Min oscillator, a prototypical example of a bacterial self-organizing system (Lutkenhaus, 2008). The Min system consists of three proteins, the ATPase MinD, the cell division inhibitor MinC and the topological factor MinE. Their spontaneous pole-to-pole oscillations ensure that the FtsZ ring forms precisely at the middle of the cell where the concentration of the cell division inhibitory complex MinCD is the lowest on time average. A large body of experimental and theoretical work has shown that the oscillatory pattern of the MinCD complex is driven by interlinked interactions between MinD, MinE and the membrane. Despite this fundamental understanding, there is, however, no widely accepted mechanism as the various published mathematical models present notable mechanistic differences (Howard and Kruse, 2005; Kruse *et al.*, 2007). Quantitative analysis of MinD oscillation should provide valuable information for model discrimination and future theoretical analysis.

Exponentially growing *E. coli* cells expressing MinE and YFP-MinD from a plasmid (after induction with 10 μ M of IPTG for 4 h) were placed onto M9-maltose agarose-padded slides (containing 10 μ M IPTG), and imaged at 37°C every 2.5 s for 20 min (Movie S2). From these time-lapse sequences, we constructed 2D and 3D kymographs of YFP-MinD dynamics over time ($n = 166$ cells); Fig. 4A shows examples for a representative cell. For each cell, we also built a 1D-profile by subtracting the integrated intensity in one cell half from the intensity in the other and normalizing by the total intensity (Fig. 4B). This profile normalizes for variation in the total amount of YFP-MinD among cells, and can be easily analysed automatically using the Fourier transform (Fig. 4C), yielding the relative amplitude (which is the fraction of MinD molecules involved in the oscillation) and the frequency (period) of the oscillations in each cell. We found that the period and the YFP-MinD fluorescence intensity show no dependence on cell length (Fig. 4D, E), consistent with previous work (Meacci and Kruse, 2005). Interestingly, however, the relative amplitude markedly increases with increasing cell length (Fig. 4F). Because the data are normalized for

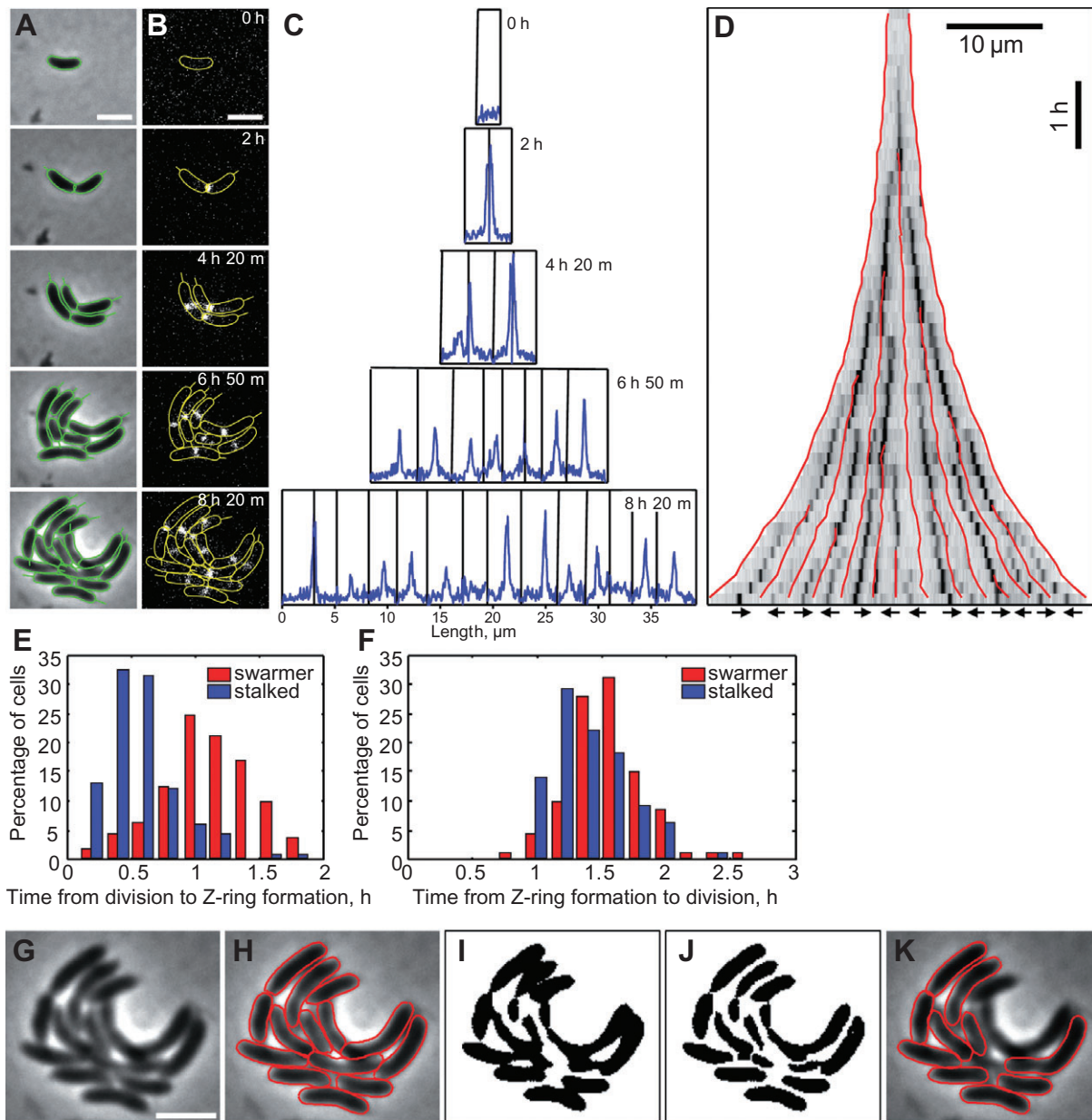


Fig. 3. Tracking bacteria over multiple generations and the timing of FtsZ ring positioning. *C. crescentus* cells expressing FtsZ-YFP under the control of vanillic acid-inducible promoter P_{van} (strain MT196) were grown in M2G medium with vanillic acid for 4 h before imaging for 10 h on agarose pads containing the same medium.

A. The progeny of one cell outlined in a time-lapse series of images. Bars: 2 μ m.

B. The same contours overlapped with FtsZ-YFP signal.

C. Corresponding fluorescence profiles normalized by segment area of all the progeny, displayed by joining the poles created at each division. D. Kymographic representation of the FtsZ-YFP signal with the intensity shown as shades of grey and the cell boundaries as red lines. Arrows at the bottom indicate the old-to-new-pole orientation of the cells.

E. Distributions of the time gaps between cell division and the moment of FtsZ-YFP localization near the cell centre for stalked and swarmer cells, as determined by MicrobeTracker.

F. Distributions of the time gaps between the moment of FtsZ-YFP localization near the cell centre and the moment of cell division for stalked and swarmer cells.

G–K. Demonstration of the effectiveness of cell outline identification in time-lapse series.

G. Original phase contrast image showing a cell cluster generated after growth and division on the pad (as in A).

H. Same image outlined using information from the previous time points.

I. Same image processed by thresholding only.

J. Same image processed using thresholding and edge detection.

K. Cells detected using thresholding and edge detection but without information from the previous frame. Some cells could not be resolved because of cell boundaries not being visible enough at this cell density.

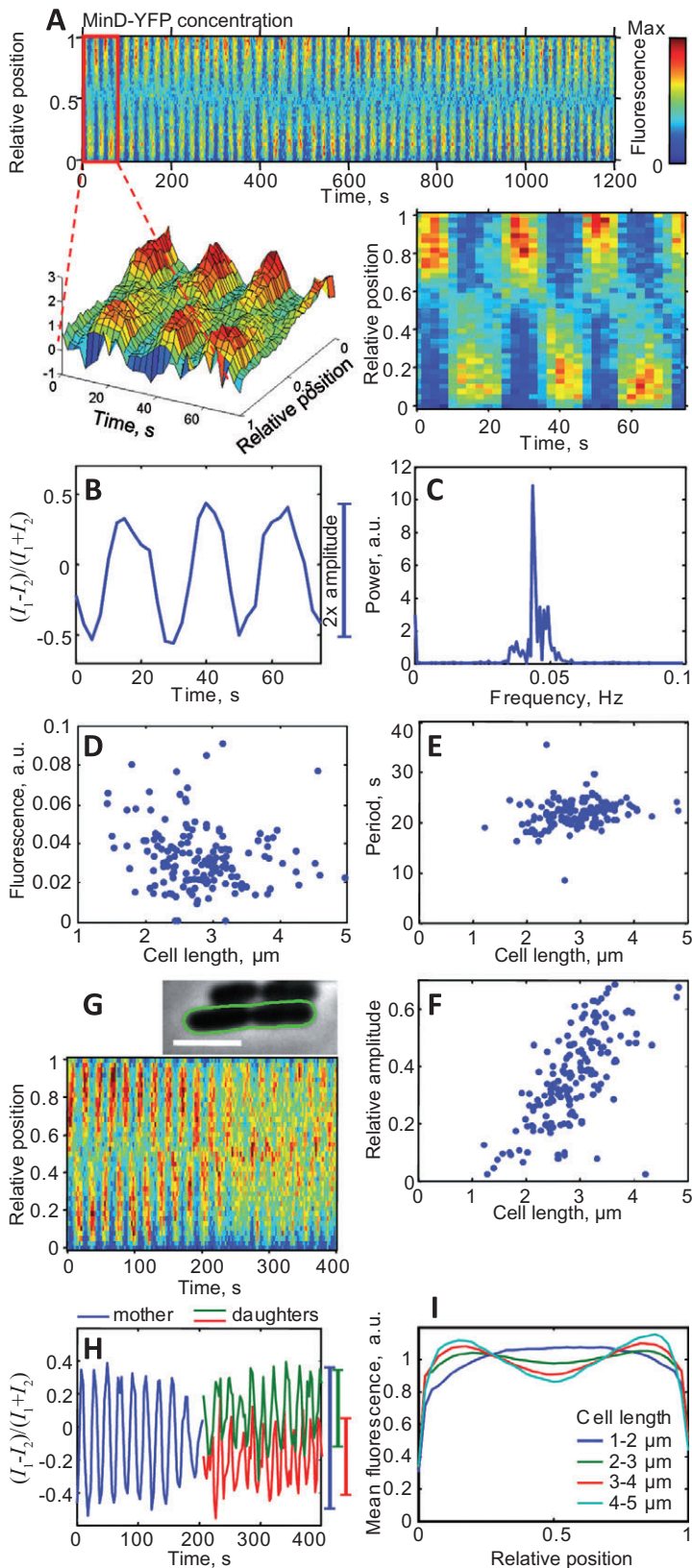


Fig. 4. Dependence of MinD oscillation dynamics on cell length. For these time-lapse experiments, YFP-MinD synthesis was induced from the *lac* promoter P_{lac} in *E. coli* cells (strain MC1000/pWM1409/pFx40) with 10 μM IPTG for 2 h before imaging on M9-maltose pad containing the same concentration of IPTG.

A. Kymographic representation of YFP-MinD localization in a single randomly selected cell imaged for 20 min at 2.5 s interval. Signal intensity was normalized by the area of each segment. The length of the cell was normalized to 1 at each time point; the actual length increased by about 10% during the experiment. The initial 75 s segment of the kymograph is shown below in 2D and 3D representations.

B. Relative cell length-independent 1D profile of the MinD-YFP oscillations defined as the integrated intensity in one half of the cell (I_1) minus the integrated intensity in the other half of the cell (I_2) divided by the total intensity (I_1+I_2). Only the initial 75 s sequence for the cell in (A) is shown. The bar on the right indicates the limits of oscillations, which define the amplitude.

C. Power spectrum of the relative 1D signal for the same cell, defined as the square of Fourier-transformed signal. The peak at zero corresponds to the offset of the mean level, whereas the peak at about 0.045 Hz corresponds to the main frequency of the oscillations.

D. The dependence of YFP-MinD concentration on cell length. The data from a single representative experiment ($n = 164$ cells) were analysed to control for the concentration of MinD as a possible mediator of the oscillation parameters.

E. Dependence of the oscillation period on cell length for the cells for the same experiment as in (D). Infrequent outliers typically correspond to misdetections when no oscillations were present. In these particular cases, the amplitude was low and the frequency random, coming from the strongest noise harmonic. The length was defined as the mean length of the cell during the experiment. The cells that divided during the experiment were removed from consideration.

F. Dependence of the relative amplitude of the oscillations (computed by integrating the largest peak in the spectrum) on cell length ($n = 164$ cells).

G. Kymograph of a cell that divided during the time-lapse sequence. Oscillations with reduced amplitude are visible (as yellow colour instead of alternating red and blue) after the septum closing event. The intensity coding is the same as in (A).

H. A 1D oscillation profile for the cell in (G) with the bars indicating the limits of oscillations for the mother (blue) and two daughter cells (red and green), showing the decrease in the amplitude after division. Bar in phase contrast image: 2 μm .

I. The profile of YFP-MinD averaged over time as a function of relative cell length. The profiles were calculated for each cell and averaged for the groups of cells falling into four intervals of cell length.

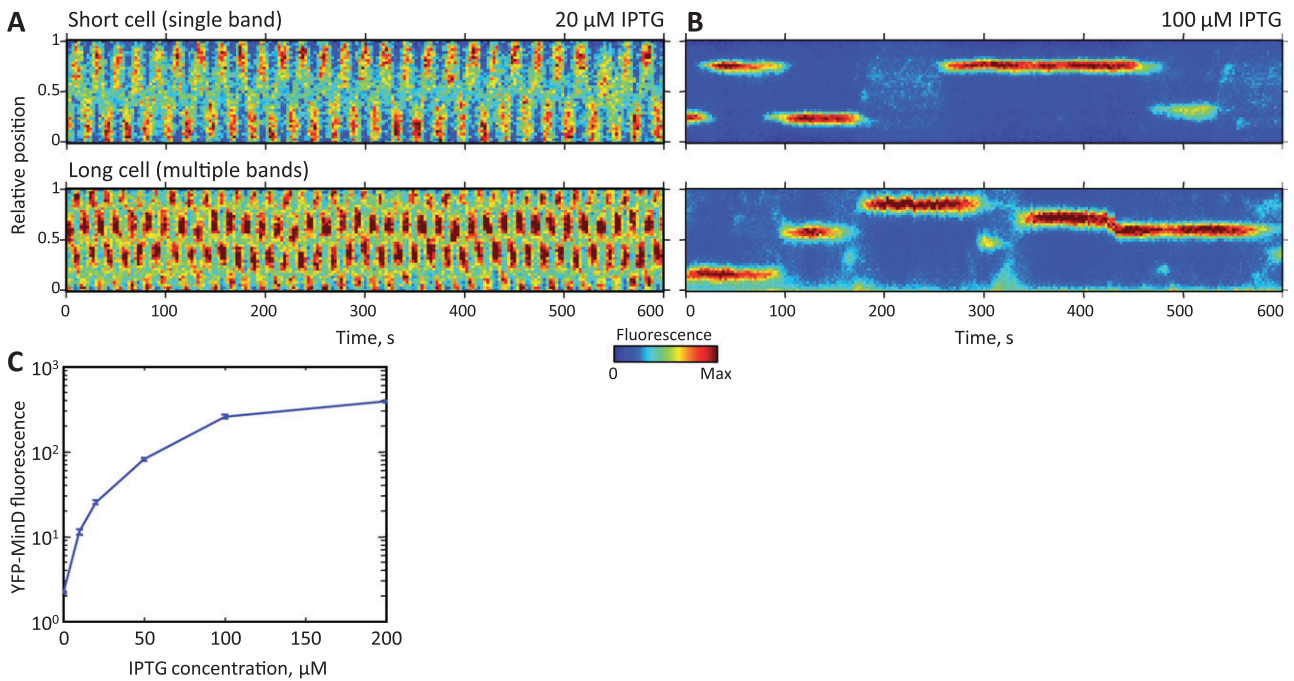


Fig. 5. Dependence of MinD dynamics on protein concentration. Here Δmin cells expressing YFP-MinD and MinE from an IPTG-inducible promoter on a plasmid (strain CJW3672) were imaged while being induced with different concentrations of IPTG. The cells were grown in M9-glycerol, preinduced with IPTG for 4 h and imaged on agarose-padded slides containing M9-glycerol and IPTG at 3 s (20 μ M IPTG) or 2.5 s (100 μ M IPTG) intervals.

A. Typical examples of cells imaged at 20 μ M IPTG showing oscillations (top: cell with a single YFP-MinD band, bottom: elongated cell with multiple YFP-MinD bands).

B. Typical examples of cells imaged at 100 μ M IPTG showing stochastic switching of YFP-MinD signal (top: cell with a single YFP-MinD band, bottom: elongated cell with multiple YFP-MinD bands).

C. Plot of YFP-MinD fluorescence intensity as a function of IPTG concentration after 4 h induction.

the total cellular level in YFP-MinD, our findings indicate that the fraction of total YFP-MinD molecules participating in the oscillation increases with cell size. This positive correlation predicts that division will be followed with reduced oscillation amplitudes in daughter cells. This was apparent in the few cells that divided during the time-lapse experiment. Figure 4G–H shows one such example in which the oscillations in a mother cell change into oscillations of smaller relative amplitude in the daughter cells. Smaller oscillation amplitudes in small cells produce weaker depletion of the amount of MinD at midcell (Fig. 4I), hence favouring FtsZ ring formation or stabilization in longer cells.

A recent study showed that the oscillatory state of MinD is a property of long cells whereas in cells shorter than 2.7 μ m, MinD resides in one half of the cell often for extended period of time until it stochastically shifts to the other half (Fischer-Friedrich *et al.*, 2010). This led to the proposal that cells have to reach a critical size to switch from stochastic MinD shifting to the oscillatory regime. Surprisingly, we found no evidence of stochastic shifting in short cells. Rather, short cells exhibited similar oscillation periods as long cells (Fig. 4E). We noted two important differences in experimental conditions between the two

studies. In Fischer-Friedrich *et al.* synthesis of plasmid-encoded MinE and fluorescently tagged MinD were induced with saturating concentration of IPTG (200 μ M) in a $\Delta min lacI^q$ background, whereas we used a lower concentration of IPTG (10 μ M) and a min^+ background. We therefore examined the distribution of YFP-MinD over time in a $\Delta min lacI^q$ background (strain CJW3672, which expresses IPTG-inducible YFP-MinD and MinE from a plasmid) after induction with varying concentrations of IPTG. At low concentration of IPTG (20 μ M), YFP-MinD exhibited normal oscillatory pattern in this background (Fig. 5A, Movies S3 and S4). At concentration of 100 μ M and above, YFP-MinD often remained localized on one side of the cell for extended periods of time, with occasional, and apparently random, shifting to the other half in cells of normal size (Fig. 5B, Movies S5 and S6). Elongated cells, which were common given the absence of MinC (also causing a minicelling phenotype), displayed the same trend with regularly spaced YFP-MinD bands oscillating at 20 μ M IPTG while shifting stochastically at 100 μ M IPTG and higher (Fig. 5A and B Bottom; data not shown). We also occasionally observed cells with diffuse (delocalized) YFP-MinD signal at high IPTG concentrations (data not shown).

Because YFP-MinD and MinE were co-expressed from an operon on the plasmid, we expect that higher concentration of IPTG results in elevated levels of both YFP-MinD and MinE without affecting their ratio. From fluorescence measurements of YFP-MinD, we estimate an approximate 10-fold increase in YFP-MinD concentration between 20 and 100 μM of IPTG (Fig. 5C). These findings suggest that the transition between the regular oscillatory regime and stochastic shifting is dependent on the overall concentration of Min proteins.

In sum, our quantitative analysis shows that the robustness of the Min system with respect to fluctuations in Min protein levels is limited to a range. At high protein concentration, the system shifts to a regime in which clusters of MinD demonstrate 'stochastic shifting' throughout the cell, which is inappropriate for division site control. We also show that under the normal oscillatory regime, the relative amplitude of oscillation (i.e. the fraction of MinD involved in the oscillation) and hence the depletion of MinD at midcell increases with cell length (Fig. 4F, I). The system has thus evolved to be maximally effective in selecting the division site when cells reach an appropriate size.

Identifying and tracking spots: replication and segregation dynamics of chromosomal origins

An ever-expanding number of identified components localize in relatively small, often diffraction-limited clusters at defined positions inside bacterial cells, appearing as foci in fluorescence images. These include chromosomal loci, mRNAs, plasmids, cell cycle regulators, receptor clusters and replication machinery to just name a few. Therefore, an important task when studying intracellular organization is to track the position of such foci in time and space. This task can be performed using the accessory program SpotFinder, which we demonstrate here by tracking the process of separation of chromosomal origins of replication in *C. crescentus*. Because the control of replication and the mechanism of chromosome segregation are only partially known in bacteria, it is important to add quantitative insight into the characterization of these essential processes.

Several reports have suggested that the cytoskeletal protein MreB contributes to chromosome segregation in several bacteria (Kruse *et al.*, 2003; 2006; Soufo and Graumann, 2003; Srivastava *et al.*, 2007; Madabhushi and Mariani, 2009) including *C. crescentus* (Gitai *et al.*, 2005; Shebelut *et al.*, 2009). However, this finding remains controversial with *E. coli* and *Bacillus subtilis* studies concluding the opposite (Formstone and Errington, 2005; Karczmarek *et al.*, 2007; Bendezu & de Boer, 2008). A popular method to examine the effect of MreB on processes of interest such as chromosome seg-

regation is to use the MreB inhibitor A22. A22 treatment affects the shape of the cells by disrupting the MreB cytoskeleton (Gitai *et al.*, 2005) and has the adverse effect of reducing cell growth independently of MreB (Karczmarek *et al.*, 2007; Takacs *et al.* 2010), complicating interpretation. We show here how our program can easily take into consideration these effects. In this experiment, we used a *C. crescentus* strain carrying fluorescently labelled ParB protein (CFP-ParB, strain MT190), which binds to the *parS* sequence close to the chromosomal origin of replication (Mohl and Gober, 1997). In *C. crescentus*, the chromosomal origin and hence ParB localize at the old-pole before replication and segregation. Shortly after replication is initiated, one of the duplicated origins rapidly segregates to the new-pole, resulting in bipolar ParB foci (Jensen and Shapiro, 1999; Mohl *et al.*, 2001). Swarmer cells were isolated and resuspended in liquid medium containing or lacking A22 (10 $\mu\text{g ml}^{-1}$) to resume cell cycle progression in a synchronous fashion. Cells were then imaged at regular time intervals in three independent experiments, and CFP-ParB foci and their position within cells were automatically identified at each time point using SpotFinder (Fig. 6A).

Almost all untreated cells displayed bipolar CFP-ParB foci after 45 min of growth following synchrony whereas less than half of A22-treated cells had bipolar foci (Fig. 6A). This difference was due to a pronounced delay in origin separation in the A22-treated cells (Fig. 6B), consistent with previous observations (Shebelut *et al.*, 2009). However, when the data were plotted as a function of cell area, instead of time, to take into account A22-mediated effects on both cell growth and shape, we found no difference between untreated and treated cell populations (Fig. 6C). Cell area was chosen as the best measure for cell size, although plotting the data versus cell length or estimated volume did not change the results significantly (data not shown). Thus, origin separation occurs when the cell reaches a certain size regardless of the presence of A22, suggesting that MreB does not play a significant role in origin segregation in *C. crescentus*, at least not at the temporal resolution used in our experiments. This is consistent with recent studies showing that the *parS/ParB/ParA* system, likely with the assistance of other mechanisms, mediates origin segregation in this organism (Toro *et al.*, 2008; Ptacin *et al.*, 2010; Schofield *et al.*, 2010; Shebelut *et al.*, 2010). Similarly to A22, many drugs and mutations affect cell growth, in addition to perturbing cellular processes of interest. Our analysis illustrates the importance of quantitatively accounting for such secondary effect.

It is well known that DNA replication and segregation affect cell division, but experimental evidence of the reverse is generally lacking despite cell division being a major component of cell cycle regulation in mathematical

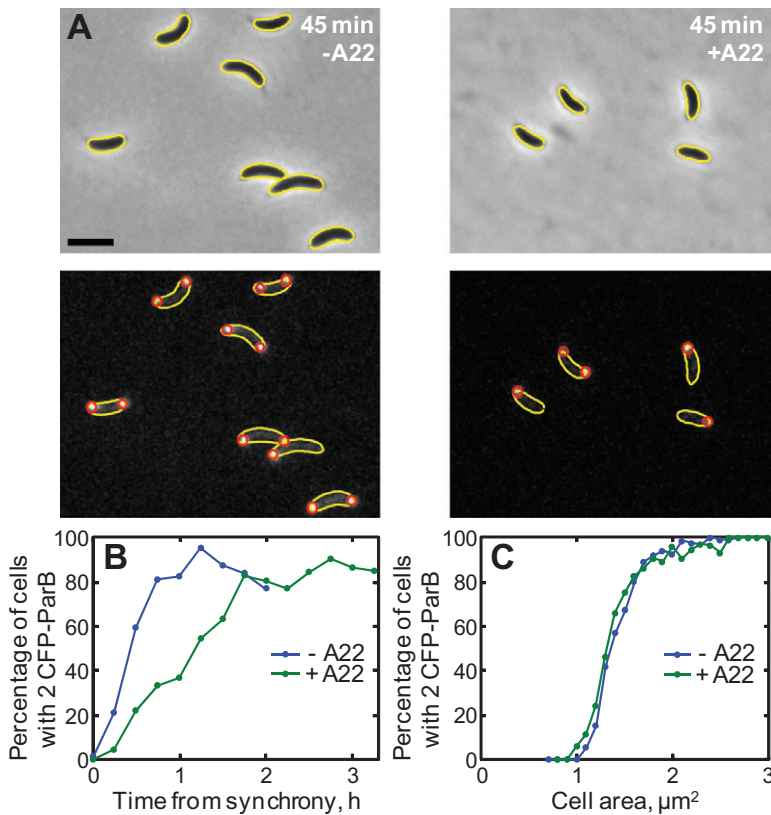


Fig. 6. Effect of A22 on origin segregation in *C. crescentus*.

A. Phase contrast and fluorescence images of MT190 cells carrying CFP-ParB after growth in liquid M2G cultures in the presence or absence of A22 ($10 \mu\text{g ml}^{-1}$) for 2 h after synchrony. Cell outlines (yellow) and CFP-ParB foci (red) detected by SpotFinder are shown. Bar: $2 \mu\text{m}$.

B. Plot showing the percentage of untreated and A22-treated cells with two visible origins of replication as a function of time after synchrony.

C. Plot showing the percentage of untreated and A22-treated cells (same as in B) with two visible origins of replication as a function of cell area.

models (Li *et al.*, 2009). Because MicrobeTracker can use information from previous time points to identify cell outlines from time-lapse sequences, it also performs remarkably well with cells blocked for cell division even as they filament, twist and touch each other during growth on agarose-padded slides (Fig. 7A). We used this unique ability to examine the role of cell division in origin replication and segregation dynamics in *C. crescentus*. For this, we used a *cfp-parB*-expressing strain carrying *ftsZ* under the control of the xylose-inducible promoter P_{xyi} . After growth in xylose, swarmer cells were isolated, allowed to resume growth on M2G-agarose padded slides lacking xylose (to turn off *ftsZ* expression), and imaged at 5 min intervals for up to 20 h. Depletion of FtsZ and inhibition of cell division were immediate because FtsZ is degraded in the swarmer cell stage (Kelly *et al.*, 1998). At each time point, the cells were outlined and CFP-ParB spots were identified using MicrobeTracker and SpotFinder respectively (the outline of a selected cell is shown in Fig. 7A). The positions of CFP-ParB spots (i.e. chromosomal origins) were plotted in absolute coordinates along the cell body relative to the cell centre, as well as in relative coordinates extending from -0.5 at the old-pole to 0.5 at the new-pole, either as a function of time (Fig. 7B, top) or cell length (Fig. 7B, bottom).

The first striking finding was a surprising cellular asymmetry in origin replication/separation events in filamenting

cells. We expected that following the first round of replication and segregation, the old-pole and new-pole origins would replicate and segregate fairly synchronously generating four origins as they would experience the same cytoplasmic environment. These four origins would then later generate eight origins and so forth. However, there was no synchrony in origin replication/separation and even more surprisingly, there was a strong bias of replication and segregation occurring from the old-pole origin for the first 16 h (~ 9 replication events; Fig. 7B, Movie S7). To quantify this bias, we determined the frequency of origin separation occurrences for each origin. We found that the second replication/segregation event occurred 94% of the time from the old-pole origin, for only 6% of occurrence from the new-pole origin ($n = 36$ cells; Fig. 7C). This observation is consistent with very recent work showing that this asymmetry can be achieved by a gradient in phosphorylation of the DNA repressor CtrA (Chen *et al.*, 2010).

Preferential replication/segregation from the old-pole origin remained pronounced in the third replication event and persisted, although to a lesser extent, up to about the seventh replication/segregation event despite the increasing number of internal origins with each replication (Fig. 7C). Thus, all origins are surprisingly not equal; instead the origin located at the old-pole is responsible for most replication/separation events while the other origins remain largely silent in the absence of division. This

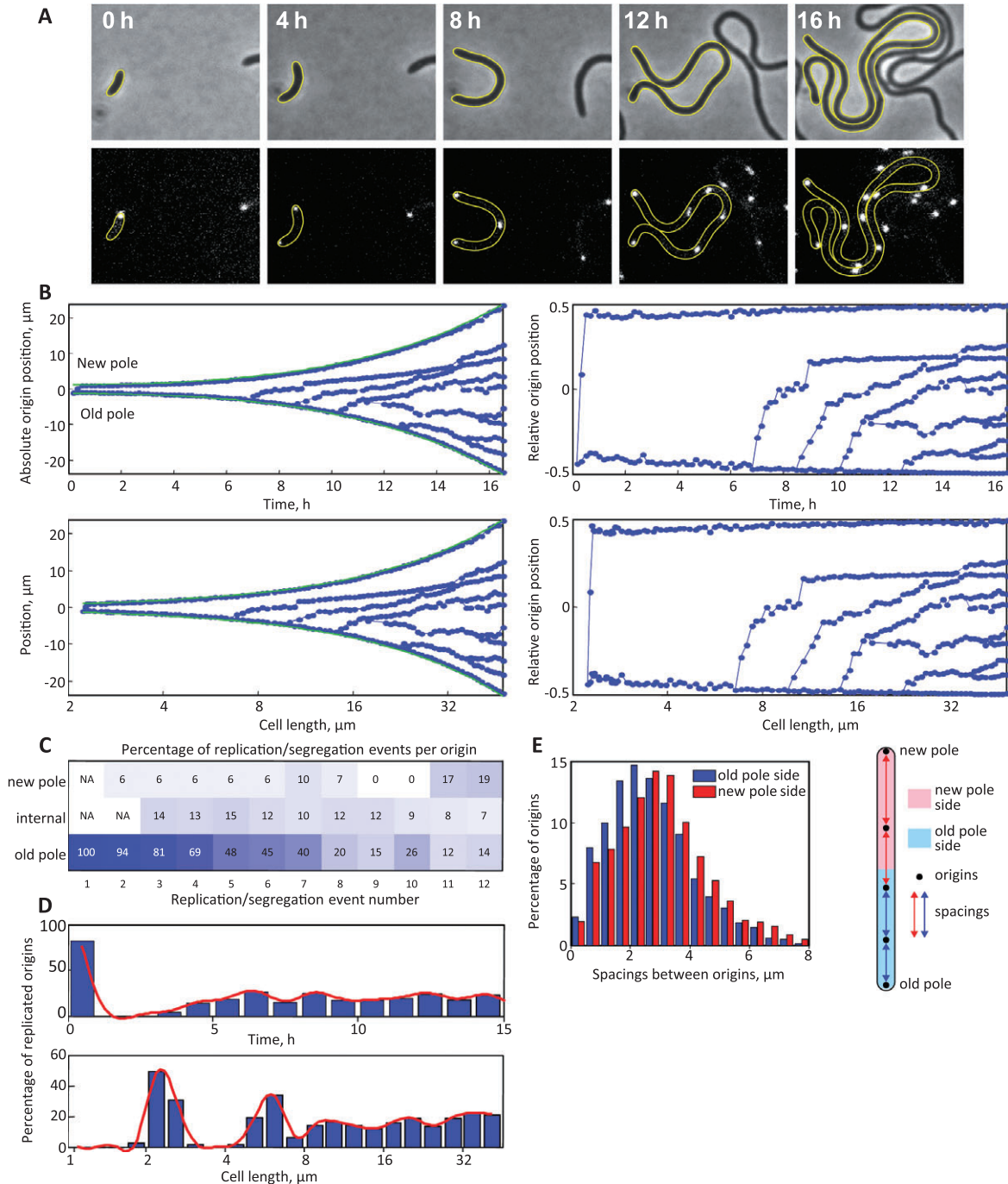


Fig. 7. Dynamics of origin replication and segregation in *C. crescentus* cells blocked for cell division. In this experiment, CJW3673 cells (CB15N *ftsZ::P_{xyl}-ftsZ parB::cfp-parB*) were depleted of FtsZ following synchrony, after which CFP-ParB was imaged by time-lapse microscopy.

A. Examples of a representative filamenting cell outlined by MicrobeTracker at selected time points.

B. For the same cell, the positions of chromosomal origins (using CFP-ParB as a proxy) are shown over time inside the cell in absolute (left) and relative (right) coordinates. The bottom graphs show the same, but plotted versus the logarithm of cell length to compensate for the differences in growth rate during the experiment. Green lines outline the length of the cell.

C. Segregation bias shown for all cells in a single representative experiment (36 cells). Here the replication and separation events of origins were sorted chronologically for each cell, and the fractions of such events for the old-pole, new-pole or internal origins are shown in percent.

D. Probability of origin replication/segregation events for all cells in the same experiment (fraction of origins that have replicated) as a function of time (top) and cell length (bottom).

E. Distribution of the spacings between chromosomal origins. The spacings were labelled based on the location of their centres in the cell (see schematic on the right) to examine whether there was a bias between the old-pole and new-pole sides of the cell.

indicates a robust cell polarity in origin replication and segregation. Eventually (after > 8 replication/separation events), the bias was lost and all origins, internal or polar, displayed similar percentage of replication/segregation events (Fig. 7C).

After the first replication event and a following lag, the probability of origins to replicate and separate seemed relatively constant when examined over time (Fig. 7D). But, when examined as a function of cell length, this probability clearly peaked at certain cell sizes, such as about 2.5, 6 and 9.5 μm , after which the dependence on cell size washed out and reached a constant (Fig. 7D). Thus, origin replication and segregation remarkably continue to cycle in accord to cell size at least for some time in the absence of cell division and cell compartmentalization.

The filamentous cells were able to redistribute chromosomes along their length, although the distribution of spacing between origins was wide (Fig. 7E). The location of the origins, whether closer to the new-pole or the old-pole, did not affect the distribution, except for a very slight shift towards shorter spacing values for origins closer to the old-pole (Fig. 7E), likely because of on-going segregation events.

Next, we analysed the motion behaviour of the origins. The polar origins did not move, consistent with their attachment to polar PopZ clusters (Bowman *et al.*, 2008; Ebersbach *et al.*, 2008) [except for an occasionally noticeable and transient detachment around the moment of replication initiation (Bowman *et al.*, 2010)], whereas most non-polar (internal) origins exhibited discernable motility. We determined three distinct regimes of motion in filamenting cells (Fig. 8A; see *Experimental procedures*). The first one, which we called directed motion, was defined as the regime of high velocity immediately following the moment of origin duplication and separation (Fig. 8B). The next regime, called diffusive motion, was defined as a high diffusion regime with intermediate velocity, which followed the directed motion. Surprisingly, a substantial fraction (~ a fifth) of internal origins followed a third regime, termed stabilized regime, which was characterized by both very low velocity and very low diffusion (Fig. 8D). We have interpreted the directed motion regime as active motion by cellular machinery (presumably the ParAB system). The diffusive regime likely represents origins that are unattached to the cell wall, although restricted to a fraction of the cell volume probably by neighbouring chromosomes (as polymers do not easily mix). This regime is likely similar to the reduction in the origin segregation velocity observed in wild-type cells (Viollier *et al.*, 2004). However, this phase persists much longer in filamenting cells, indicating the importance of polar attachment in stabilizing the origin position. The very low diffusion of the stabilized regime and its zero relative velocity (i.e. with an absolute velocity equal to the velocity

of the cell wall at that position assuming uniform growth) suggests an indirect attachment to the cell wall.

In sum, in the absence of cell compartmentalization, origins display different types of motion that likely reflect their interaction with cellular components. Perhaps more importantly, our analysis of FtsZ-depleted cells reveals a position-dependent bias in replication/segregation potential for chromosomal origins. The polarity of this spatial mechanism is reset with each division. We also found that the cell has a cell size-sensitive mechanism that triggers DNA replication and segregation.

Footnote

To facilitate its use by biologists, MicrobeTracker comes with a user-friendly graphical interface that allows the user to perform automated tasks while visualizing intermediate results with the options of complete automation and manual intervention if needed. The package is released under the GNU General Public License (GPL) and can be downloaded free of charge from <http://www.microbetracker.org> together with a number of other MATLAB-based tools that we developed to aid with data analysis. A detailed description of the interface and tools is provided in the online Manual. Automated, quantitative single-cell analysis using MicrobeTracker should prove useful to microscopy-based studies of not only bacteria but also higher organisms (e.g. *Schizosaccharomyces pombe*, *Caenorhabditis elegans*, etc.). For instance, we have successfully tested the software to measure the properties of *Drosophila melanogaster* larvae motility during chemotaxis (data not shown).

Experimental procedures

Bacterial strains and growth conditions

Caulobacter crescentus cells were grown in M2G medium supplemented with 1% PYE in the presence of appropriate antibiotics (kanamycin, gentamycin). Log-phase cultures were used for all experiments. Expression from P_{xyI} and P_{van} was induced by adding to the medium 0.3% xylose and 500 μM vanillic acid respectively. The synchrony was performed as described (Evinger and Agabian, 1977). *E. coli* cells were grown in M9 minimal medium supplemented with 1 mM MgSO_4 , 0.2% casamino acids, 50 μM thiamine, 0.2% of either maltose or glycerol in the presence of appropriate antibiotics (ampicillin, chloramphenicol). Strains and plasmids are listed in Table S1.

Microscopy

Cells were imaged using a Nikon Ti microscope equipped with a 100 \times phase-contrast objective and an Andor iXon EMCCD camera. The cells were immobilized on 1% agarose pads with the appropriate medium. Individual images (i.e. that are not part of a time-lapse series) were obtained at room

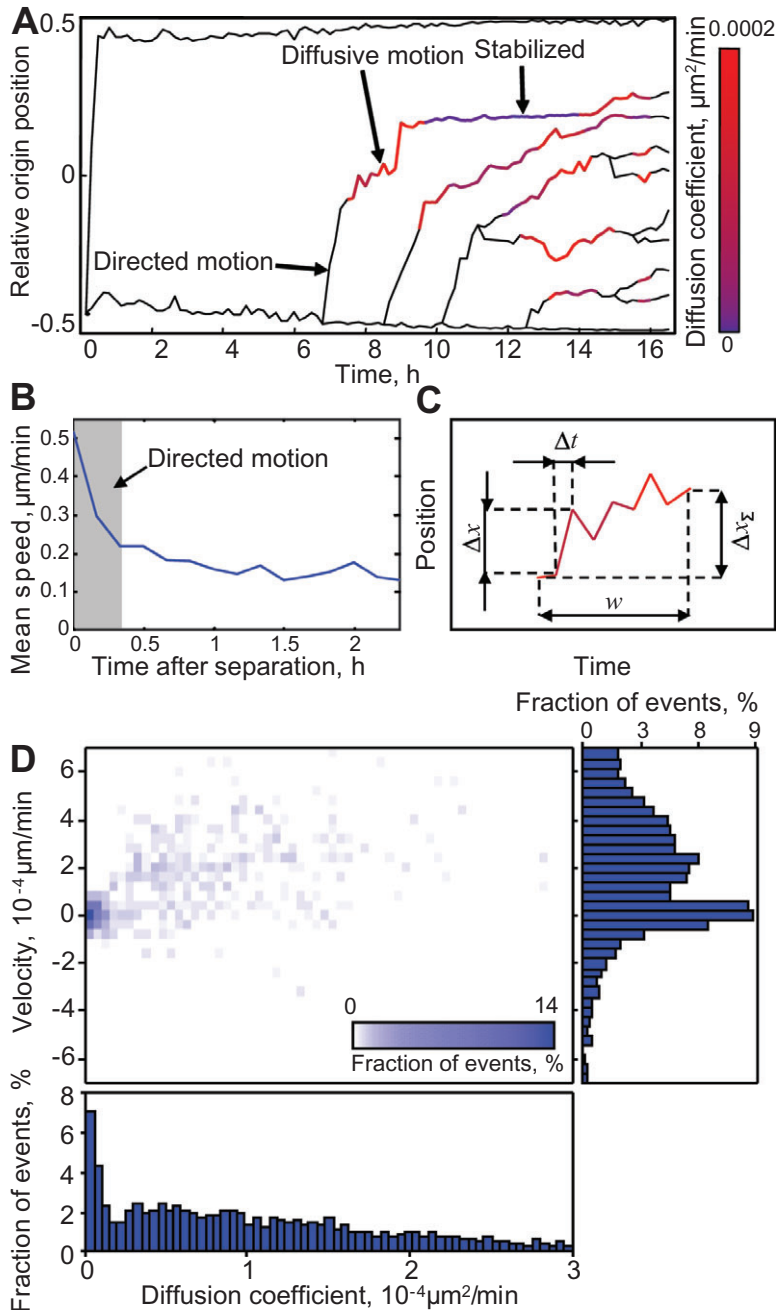


Fig. 8. Motion analysis of the origins.

A. Motion analysis of the origins for the cell in Fig. 7A and B. Three distinct regimes were identified. 'Directed' motion was defined as the high speed regime immediately following replication/separation events (see also panel B). The other motion types were analysed based on diffusion analysis. A sliding window (of 10 time frames long) was placed on the origin tracks and the motion characterized within each position of the window as random motion with the diffusion coefficient D superimposed with a drift velocity V (panels C and D). The diffusion coefficient is shown as line colour.

B. Definition of 'directed' motion. This motion corresponds to the regime of high speed immediately following origin separation (shaded area).

C. Diffusion analysis of the origins. The tracks were analysed based on diffusion analysis: a sliding window was placed on the origin tracks and the motion characterized as a random motion with the diffusion coefficient D superimposed with a drift velocity V , calculated within each window using the shown variables (see *Experimental procedures*).

D. Histograms of this diffusion analysis. Two distinct peaks corresponding to diffusive motion and the stabilized state are clearly seen on the 2D histogram and on its projections to both V and D axes. Based on the analysis, we identified two distinct regimes: 'diffusive motion' is characterized by intermediate velocity and high diffusion, whereas 'stabilized state' is characterized by both low velocity and diffusion.

temperature immediately after cell immobilization, whereas time-lapse imaging was performed at 30°C (*C. crescentus*) or 37°C (*E. coli*) using a heated objective.

MicrobeTracker program

The program proceeds in two stages. In the first one, the program applies a set of pixel-based operations to the images in order to segregate and crudely outline individual cells, producing an initial guess of their shape. In the second stage, one of two algorithms based on active contour models (Kass *et al.*, 1988) is used to refine each cell

outline (see *Supporting information* for technical description of each algorithm and consult the program website <http://www.microbetracker.org> for the operation manual).

The first stage consists of pixel-based operations as follows. First, the program performs thresholding, isolating cells or cell clusters from background, supplemented with edge detection in order to separate cells within cell clusters. While thresholding is the most widely used technique to detect contrasting objects (such as cells) on relatively uniform background, it frequently fails in the case of uneven cell or background intensity, which can occur because of non-uniform illumination, uneven surface of immobilization, differences in probe

levels, etc. In addition, thresholding frequently does not resolve touching cells, as illustrated in Fig. 1A. Using this method alone can cause a significant loss of data and requires more manual control. These issues are especially problematic for time-lapse measurements of dividing cells as growth and division of immobilized cells lead to cell clusters. Edge detection (Fig. 1A) solves many of these problems (Fig. S1; see also *Supporting information*). In most cases, applying edge detection is sufficient, but when it is not (which is determined by a segmented region being larger than a certain size limit), a routine based on the watershed transform (Meyer, 1994) is applied to separate cells along the most likely path and is repeated until each cell is smaller than the size limit (see *Supporting information*). At the end of this first stage, the program produces guesses for the cell shapes.

In the next stage, refined cell contours are obtained using one of the two algorithms of active contour models implemented in MicrobeTracker. For either algorithm, the shape of an individual cell is described by a contour, which is adjusted smoothly until it converges to the cell shape through the action of image forces (Fig. 1B) (see *Supporting information* for an exact description of the forces used). Another common property of the two algorithms is that the contour must obey internal constraints. The nature of these constraints and their exact parameterizations (i.e. the ways of describing the contours with sets of parameters) are different for the two alternative algorithms. The selection between these algorithms is made by the user.

One algorithm is an implementation of the Point Distribution Model (PDM) (Cootes *et al.*, 1995) (see *Supporting information*). For each cell type that is substantially different in shape, this method uses a 'training' procedure to automatically find a small number of descriptors describing possible cell shapes and therefore imposing constraints on them. The image forces are then linearly projected onto the reduced set of descriptors. This method is fast, but it is limited to spaces of cell shape that can be linearly transformed one into another (it is unable to work with filamentous or highly curved cells), and lacks the ability to manually adjust the constraints without retraining.

An alternative to PDM is an active contour algorithm with manually preset constraints (Manually Constrained Contour – model). This Manually Constrained Contour method assumes that a cell is rod-shaped with approximately uniform width and rounded poles and parameterizes its shape by explicit coordinates of a set of points along the contour sampled at equal step. This method is slower than the PDM but is able to outline elongated and filamentous cells, as well as a wide range of cell types (or species) as long as they have a defined long cell axis. Because of its versatility, this algorithm was used in all biological examples described in this study and typically is the preferred setting in MicrobeTracker. Both variants of the active contour model are 'off-lattice' methods and therefore can provide precise subpixel positioning of cell contours.

SpotFinder program

The SpotFinder program is designed to identify round or diffraction-limited spots and to position them in the 2D cell co-ordinate system created by MicrobeTracker. This program combines spatial 2D filtering and a new algorithm, which we

call 'ridge removal', to find objects of the right size and to remove elongated structures respectively (see *Supporting information*). The maxima of the filtered image are used as original guesses of spot positions to fit the shape of each spot with a Gaussian plus a constant for the background (Fig. 1E). The program then keeps those objects with a good fit, intensity above the background and width within a defined range in order to discriminate 'real' spots from noise. The limits of the 'good fit' are set by the user in a quick training procedure, in which the user goes through several cells picking 'real' spots. During the fit, the position of the spot centre is allowed to vary in the vicinity of the original guess in order to determine the coordinates of the spots' centres at subpixel resolution (see *Supporting information*).

Motion analysis of chromosomal origins of replication

The origins of replication were detected with SpotFinder and were connected between time frames using a semi-manual code that attempts to find the best match between the spots on consecutive frames, and then allows the user to modify the assignments in infrequent complicated cases, such as misdetection of origins.

The motion of the origins of replication (CFP-ParB foci) was analysed assuming two independent linearly additive components – constant drift motion and diffusive random walk (except for the directed motion that occurs too fast – in too few time points – see below). The analysis was performed using a sliding window of width w in time, consisting of several intervals Δt between images ($w = 10$ in our case, Fig. 8B). For graphical representation purposes (Fig. 8A), the obtained values were assigned to the central segment of the interval.

We first determined the relative displacement of the origin between frames Δx (Fig. 8C) and then calculated the displacement of the origin relative to the cell wall ΔX by multiplying the relative displacement by cell length. Calling the length of the cell at i -th time point L_i and the position of the origin p_i , $\Delta x_{i+1/2} = p_{i+1}/L_{i+1} - p_i/L_i$ and $\Delta X_{i+1/2} = \Delta x_{i+1/2}(L_{i+1} + L_i)/2$. Note that the displacement ΔX calculated this way is relative to the nearest cell wall point and is different from a simple difference in absolute positions of the origins between frames $p_{i+1} - p_i$, which would indicate the displacement relative to the old-pole of the cell. Here we are interested in the motion relative to the cell wall, and not the pole, which may be very distant in a filamentous cell.

Once we obtained the displacements, we estimated the drift velocity and diffusion in a sliding window of width w in time consisting of several time intervals (of duration Δt each, see Fig. 8C). The drift velocity was calculated simply by averaging the displacements within the window and the diffusion from Fick's law using the displacements minus the effect of the drift:

$$V = \langle \Delta X_i / \Delta t \rangle_w$$

$$D = \langle (\Delta X_i - V \Delta t)^2 / 2 \Delta t \rangle_w$$

This analysis was performed for all cells (36 in total) in a single representative experiment. It allowed us to separate the diffusive motion regime and the stabilized regime. The two regimes were separated based on histograms of drift

velocity and diffusion, which show two distinct peaks, a tight one around zero V and D , corresponding to the stabilized regime, and a broad one around $V \sim 2 \cdot 10^{-4} \mu\text{m/s}$ and $D \sim 10^{-4} \mu\text{m}^2/\text{s}$ corresponding to the diffusive regime (Fig. 8D).

The motion in the first few frames after separation cannot be accessed by this method because the window size had to be larger than the fast motion period immediately after separation. Therefore, the first mode of motion of the origins of replication inside cells – directed motion – was defined as the regime of high velocity immediately following the separation moment (Fig. 8B).

Acknowledgements

We thank S. Zucker, P. Dimitrov and M. Sneddon for help in developing the software; P. de Boer and J. Lutkenhaus for strains; P. Montero Llopis for experimental help; many members of the Jacobs-Wagner and Emonet laboratories, especially W. Schofield, P. Montero Llopis and G. Laloux, for valuable discussions; and the Jacobs-Wagner lab for critical reading of an earlier version of this manuscript. This work was funded in part by the National Institutes of Health (GM076698 and GM065835 to C.J.-W.), and the National Science Foundation (CCF-0829836 to T.E.). C.J.-W. is an investigator of the Howard Hughes Medical Institute.

References

- Ackermann, M., Stearns, S.C., and Jenal, U. (2003) Senescence in a bacterium with asymmetric division. *Science* **300**: 1920.
- Bendezu, F.O., and de Boer, P.A. (2008) Conditional lethality, division defects, membrane involution, and endocytosis in *mre* and *mrd* shape mutants of *Escherichia coli*. *J Bacteriol* **190**: 1792–1811.
- Bowman, G.R., Comolli, L.R., Zhu, J., Eckart, M., Koenig, M., Downing, K.H., *et al.* (2008) A polymeric protein anchors the chromosomal origin/ParB complex at a bacterial cell pole. *Cell* **134**: 945–955.
- Bowman, G.R., Comolli, L.R., Gaietta, G.M., Fero, M., Hong, S.H., Jones, Y., *et al.* (2010) *Caulobacter* PopZ forms a polar subdomain dictating sequential changes in pole composition and function. *Mol Microbiol* **76**: 173–189.
- Chen, Y.E., Tropini, C., Jonas, K., Tsokos, C.G., Huang, K.C., and Laub, M.T. (2010) Spatial gradient of protein phosphorylation underlies replicative asymmetry in a bacterium. *Proc Natl Acad Sci USA* **108**: 1052–1057.
- Christen, B., Fero, M.J., Hillson, N.J., Bowman, G., Hong, S.H., Shapiro, L., and McAdams, H.H. (2010a) High-throughput identification of protein localization dependency networks. *Proc Natl Acad Sci USA* **107**: 4681–4686.
- Christen, M., Kulasekara, H.D., Christen, B., Kulasekara, B.R., Hoffman, L.R., and Miller, S.I. (2010b) Asymmetrical distribution of the second messenger c-di-GMP upon bacterial cell division. *Science* **328**: 1295–1297.
- Cootes, T.F., Taylor, C.J., Cooper, D.H., and Graham, J. (1995) Active shape models – their training and application. *Comp Vis Image Under* **61**: 38–59.
- Ebersbach, G., Briegel, A., Jensen, G.J., and Jacobs-Wagner, C. (2008) A self-associating protein critical for chromosome attachment, division, and polar organization in *Caulobacter*. *Cell* **134**: 956–968.
- Evinger, M., and Agabian, N. (1977) Envelope-associated nucleoid from *Caulobacter crescentus* stalked and swarmer cells. *J Bacteriol* **132**: 294–301.
- Fischer-Friedrich, E., Meacci, G., Lutkenhaus, J., Chate, H., and Kruse, K. (2010) Intra- and intercellular fluctuations in Min-protein dynamics decrease with cell length. *Proc Natl Acad Sci USA* **107**: 6134–6139.
- Formstone, A., and Errington, J. (2005) A magnesium-dependent *mreB* null mutant: implications for the role of *mreB* in *Bacillus subtilis*. *Mol Microbiol* **55**: 1646–1657.
- Gitai, Z., Dye, N.A., Reisenauer, A., Wachi, M., and Shapiro, L. (2005) *MreB* actin-mediated segregation of a specific region of a bacterial chromosome. *Cell* **120**: 329–341.
- Guberman, J.M., Fay, A., Dworkin, J., Wingreen, N.S., and Gitai, Z. (2008) PSICIC: noise and asymmetry in bacterial division revealed by computational image analysis at sub-pixel resolution. *PLoS Comput Biol* **4**: e1000233.
- Hallez, R., Bellefontaine, A.F., Letesson, J.J., and De Bolle, X. (2004) Morphological and functional asymmetry in alpha-proteobacteria. *Trends Microbiol* **12**: 361–365.
- Howard, M., and Kruse, K. (2005) Cellular organization by self-organization: mechanisms and models for Min protein dynamics. *J Cell Biol* **168**: 533–536.
- Jensen, R.B., and Shapiro, L. (1999) The *Caulobacter crescentus* *smc* gene is required for cell cycle progression and chromosome segregation. *Proc Natl Acad Sci USA* **96**: 10661–10666.
- Karczmarek, A., Martinez-Arteaga, R., Alexeeva, S., Hansen, F.G., Vicente, M., Nanninga, N., and den Blaauwen, T. (2007) DNA and origin region segregation are not affected by the transition from rod to sphere after inhibition of *Escherichia coli* *MreB* by A22. *Mol Microbiol* **65**: 51–63.
- Kass, M., Witkin, A., and Terzopoulos, D. (1988) Snakes: active contour models. *Int J Comput Vis* **1**: 321–331.
- Kelly, A.J., Sackett, M.J., Din, N., Quardokus, E., and Brun, Y.V. (1998) Cell cycle-dependent transcriptional and proteolytic regulation of FtsZ in *Caulobacter*. *Genes Dev* **12**: 880–893.
- Kruse, T., Moller-Jensen, J., Lobner-Olesen, A., and Gerdes, K. (2003) Dysfunctional *MreB* inhibits chromosome segregation in *Escherichia coli*. *EMBO J* **22**: 5283–5292.
- Kruse, T., Blagoev, B., Lobner-Olesen, A., Wachi, M., Sasaki, K., Iwai, N., *et al.* (2006) Actin homolog *MreB* and RNA polymerase interact and are both required for chromosome segregation in *Escherichia coli*. *Genes Dev* **20**: 113–124.
- Kruse, K., Howard, M., and Margolin, W. (2007) An experimentalist's guide to computational modelling of the Min system. *Mol Microbiol* **63**: 1279–1284.
- Lam, H., Matroule, J.Y., and Jacobs-Wagner, C. (2003) The asymmetric spatial distribution of bacterial signal transduction proteins coordinates cell cycle events. *Dev Cell* **5**: 149–159.
- Li, S., Brazhnik, P., Sobral, B., and Tyson, J.J. (2009) Temporal controls of the asymmetric cell division cycle in *Caulobacter crescentus*. *PLoS Comput Biol* **5**: e1000463.
- Locke, J.C., and Elowitz, M.B. (2009) Using movies to analyse gene circuit dynamics in single cells. *Nat Rev Microbiol* **7**: 383–392.

- Lutkenhaus, J. (2008) Min oscillation in bacteria. *Adv Exp Med Biol* **641**: 49–61.
- Madabhushi, R., and Mariani, K.J. (2009) Actin homolog MreB affects chromosome segregation by regulating topoisomerase IV in *Escherichia coli*. *Mol Cell* **33**: 171–180.
- Meacci, G., and Kruse, K. (2005) Min-oscillations in *Escherichia coli* induced by interactions of membrane-bound proteins. *Phys Biol* **2**: 89–97.
- Meyer, F. (1994) Topographic distance and watershed lines. *Signal Proc* **38**: 113–125.
- Mohl, D.A., and Gober, J.W. (1997) Cell cycle-dependent polar localization of chromosome partitioning proteins in *Caulobacter crescentus*. *Cell* **88**: 675–684.
- Mohl, D.A., Easter, J., Jr, and Gober, J.W. (2001) The chromosome partitioning protein, ParB, is required for cytokinesis in *Caulobacter crescentus*. *Mol Microbiol* **42**: 741–755.
- Pham, D.L., Xu, C.Y., and Prince, J.L. (2000) Current methods in medical image segmentation. *Annu Rev Biomed Eng* **2**: 315–337.
- Ptacin, J.L., Lee, S.F., Garner, E.C., Toro, E., Eckart, M., Comolli, L.R., *et al.* (2010) A spindle-like apparatus guides bacterial chromosome segregation. *Nat Cell Biol* **12**: 791–798.
- Quardokus, E.M., and Brun, Y.V. (2002) DNA replication initiation is required for mid-cell positioning of FtsZ rings in *Caulobacter crescentus*. *Mol Microbiol* **45**: 605–616.
- Schofield, W.B., Lim, H.C., and Jacobs-Wagner, C. (2010) Cell cycle coordination and regulation of bacterial chromosome segregation dynamics by polarly localized proteins. *EMBO J* **29**: 3068–3081.
- Shapiro, L., and Losick, R.M. (2010) *Cell Biology of Bacteria*. Cold Spring Harbor, NY: Cold Spring Harbor Laboratory Press.
- Shebelut, C.W., Jensen, R.B., and Gitai, Z. (2009) Growth conditions regulate the requirements for *Caulobacter* chromosome segregation. *J Bacteriol* **191**: 1097–1100.
- Shebelut, C.W., Guberman, J.M., van Teeffelen, S., Yakhnina, A.A., and Gitai, Z. (2010) *Caulobacter* chromosome segregation is an ordered multistep process. *Proc Natl Acad Sci USA* **107**: 14194–14198.
- Soufo, H.J., and Graumann, P.L. (2003) Actin-like proteins MreB and Mbl from *Bacillus subtilis* are required for bipolar positioning of replication origins. *Curr Biol* **13**: 1916–1920.
- Srivastava, P., Demarre, G., Karpova, T.S., McNally, J., and Chattoraj, D.K. (2007) Changes in nucleoid morphology and origin localization upon inhibition or alteration of the actin homolog, MreB, of *Vibrio cholerae*. *J Bacteriol* **189**: 7450–7463.
- Stewart, E.J., Madden, R., Paul, G., and Taddei, F. (2005) Aging and death in an organism that reproduces by morphologically symmetric division. *PLoS Biology* **3**: 295–300.
- Takacs, C.N., Poggio, S., Charbon, G., Pucéault, M., Vollmer, W., and Jacobs-Wagner, C. (2010) MreB drives de novo rod morphogenesis in *Caulobacter crescentus* via remodeling of the cell wall. *J Bacteriol* **192**: 1671–1684.
- Terrana, B., and Newton, A. (1975) Pattern of unequal cell division and development in *Caulobacter crescentus*. *Dev Biol* **44**: 380–385.
- Toro, E., Hong, S.H., McAdams, H.H., and Shapiro, L. (2008) *Caulobacter* requires a dedicated mechanism to initiate chromosome segregation. *Proc Natl Acad Sci USA* **105**: 15435–15440.
- Viollier, P.H., Thanbichler, M., McGrath, P.T., West, L., Meewan, M., McAdams, H.H., and Shapiro, L. (2004) Rapid and sequential movement of individual chromosomal loci to specific subcellular locations during bacterial DNA replication. *Proc Natl Acad Sci USA* **101**: 9257–9262.
- Wang, P., Robert, L., Pelletier, J., Dang, W.L., Taddei, F., Wright, A., and Jun, S. (2010a) Robust growth of *Escherichia coli*. *Curr Biol* **20**: 1099–1103.
- Wang, Q., Niemi, J., Tan, C.M., You, L., and West, M. (2010b) Image segmentation and dynamic lineage analysis in single-cell fluorescence microscopy. *Cytometry A* **77**: 101–110.

Supporting information

Additional supporting information may be found in the online version of this article.

Please note: Wiley-Blackwell are not responsible for the content or functionality of any supporting materials supplied by the authors. Any queries (other than missing material) should be directed to the corresponding author for the article.